

Three-component modelling of O-rich AGB star winds

I. Effects of drift using forsterite

C. Sandin¹, L. Mattsson², K. L. Chubb³, M. Ergon^{4,1}, and P. M. Weillbacher⁵

¹ Department of Astronomy, AlbaNova University Center, Stockholm University, SE-10691 Stockholm, Sweden
e-mail: christer.sandin@astro.su.se

² Nordita, KTH Royal Institute of Technology and Stockholm University, Hannes Alfvéns väg 12, SE-10691 Stockholm, Sweden

³ Centre for Exoplanet Science, University of St Andrews, North Haugh, St Andrews, KY16 9SS, United Kingdom

⁴ The Oskar Klein Centre, AlbaNova, SE-10691 Stockholm, Sweden

⁵ Leibniz-Institut für Astrophysik Potsdam (AIP), An der Sternwarte 16, 14482 Potsdam, Germany

Submitted January 3, 2023

ABSTRACT

Stellar winds of cool and pulsating asymptotic giant branch (AGB) stars enrich the interstellar medium with large amounts of processed elements and various types of dust. We present a first study on the influence of gas-to-dust drift on ab initio simulations of stellar winds of M-type stars driven by radiation pressure on forsterite particles. Our study is based on our radiation hydrodynamic model code T-800 that includes frequency-dependent radiative transfer, dust extinction based on Mie scattering, grain growth and ablation, gas-to-dust drift using one mean grain size, a piston that simulates stellar pulsations, and an accurate high spatial resolution numerical scheme. To enable this study, we calculated new gas opacities based on the `EXOMOL` database, and we extended the model code to handle the formation of minerals that may form in M-type stars. We discern effects of drift by comparing drift models to our new and extant non-drift models. Compared to our recent results of C-rich stellar winds, our two new drift models based on an oxygen-rich chemistry show drift velocities that are higher by about a factor ten, that is 310–360 km s⁻¹. Our new drift model mass-loss rates are 8–20 times lower than our own non-drift models, but compared to extant models that use the same stellar parameters, our mass-loss rates are 10–420 times lower. Meanwhile, a comparison of other properties such as the expansion velocity and grain size show similar values. Our results show that the inclusion of gas-to-drift is of fundamental importance in stellar wind models driven by transparent grains such as forsterite. Assuming that the drift velocity is insignificant, properties such as the mass-loss rate may be off from more realistic values by a factor one hundred and more.

Key words. hydrodynamics – radiative transfer – stars: atmospheres – stars: AGB and post-AGB – stars: mass-loss – stars: winds, outflows

1. Introduction

Stellar winds rule the final and decisive stages of evolution of low-to-intermediate mass stars when they ascend the asymptotic giant branch (AGB). The dynamic AGB stage involves increasing luminosities, low effective temperatures, and stellar pulsations. Dust formation begins at a couple of stellar radii where temperatures are low enough to prevent the newly formed grains from evaporating, and the new dust grains absorb or scatter the radiation and in that way attain a momentum. The grains accelerate outwards and collide with particles in the gas that are dragged along as the particles drift through the same gas. Considering all the needed physics, it is a physical problem of a kind to simulate the resulting dust-driven wind where low expansion velocities are about 10 km s⁻¹ and high mass-loss rates vary from 10⁻⁸ up to, in extreme cases, 10⁻⁴ M_⊙ yr⁻¹.

Depending on what element dominates, AGB stars are either oxygen-rich (M-type stars) or carbon-rich (C-type stars). The dichotomy is reflected in stellar wind models where dust formation in a carbon-rich chemistry is more simple where mostly amor-

phous carbon forms. Other types of dust and minerals do not form in sufficient numbers to be influential.

Dust formation in an oxygen-rich chemistry is more complex. Spectra of circumstellar envelopes of M-type AGB stars show characteristic silicate features at 9.7 and 18 μm (see, e.g. Woolf & Ney 1969; Low 1970; Molster et al. 2002; Dorschner 2010; Molster et al. 2010). These features indicate that silicon-containing grains are a dominant component of the in M-type AGB stars. Crystalline silicate dust with features at 11, 23, 28, 33, and 69 μm is also seen (Blommaert et al. 2014), but the crystallinity does not appear to be correlated with the mass-loss rates (Liu et al. 2017). Various minerals form depending on the availability of elements that are part of the different minerals, including olivine, pyroxene, and iron (Gail & Sedlmayr 1999). Metallic iron, moreover, appears to be a significant component in the cosmic dust budget owing to the large iron depletion seen in the interstellar medium (Mattsson et al. 2019). Such grains can probably form in AGB atmospheres and their scattering cross-sections are typically large, so if they form in sufficient number, they may contribute to the driving of the wind. Gail & Sedlmayr (2014,

hereafter, GS14) present a refined and many ways complete approach on how to implement mineral formation in both carbon and oxygen-rich chemistries.

Höfner (2008, hereafter H08) presents first working models (DARWIN) of stellar winds in oxygen-rich chemistry. She finds that the dust scattering cross section of larger micron-sized iron-free silicates particles provide a high enough radiative pressure to drive a stellar wind. Bladh & Höfner (2012) and Bladh et al. (2013) then argue, based mostly on parameterized models of dust, that forsterite and enstatite are the most likely dust species that drive the stellar wind; they also present photometric properties of models that agree well with observations. Bladh et al. (2015) present a larger set of radiation hydrodynamic models that include non-equilibrium dust formation. The authors conclude that they can calculate mass-loss rates as well as spectra, which visual and near-IR diagnostics agree with observations. Bladh et al. (2019, hereafter B19) present the most extensive set of calculated M-type stellar wind models available this far. Whilst the stellar wind models of H08 up to B19 show agreement with observations, they are based on some assumptions that we find interesting to explore in more detail. The authors emphasize that they calculate high mass-loss rates and photometric properties that agree well with observations. They also point out that there are few free parameters in their radiation hydrodynamic models. In particular, the only such free parameter they mention is the seed particle abundance. The authors, moreover, appear to use sticking coefficients that are always set to unity (1) to form as much dust as possible, instead of using extant lower empirically based values. Additional assumptions include only modeling one (or two) dust species at a time.

Physical arguments imply that effects of drift are stronger in these winds than in carbon-rich environments (Mattsson & Sandin 2021, hereafter MS21). Only one extant study addresses effects of drift, whilst assuming very low drift velocities, lacking any "evidence" for higher values (Tosi et al. 2022). We think there is good reason to check the influence of drift on results more carefully. As we show here, drift velocities turn out to be dramatically higher in models of M-type stars than in models of C-type stars. Correspondingly, we also find dramatically lower mass-loss rates. We are – with our physically and numerically extended models – unable to reproduce the higher valued DARWIN-based mass-loss rates that the authors base their results of good agreement with observations on. Whilst more reliable observations of mass loss show higher mass-loss rates, it seems something important is missing in the picture of understanding the formation of stellar winds in M-type stars.

Extant ab initio stellar wind models that include drift are all based on a carbon-rich chemistry. Sandin & Mattsson (2020, hereafter Paper V) include frequency-dependent radiative transfer and opacity tables of both the gas and the dust, and calculate models at high spatial resolution: results indicate important differences between drift models and position-coupled (PC) models. Mass-loss rates, expansion velocities, and yields of dust are affected. An additional example of a carbon-rich model where drift is found to be an important component to understand the observations is presented in a study of grain alignment about IRC+10°216 (Andersson et al. 2022); this object shows a very high mass-loss rate, where our model nevertheless show a drift velocity that is twice as high as the expansion velocity.

We use our simulation code T-800 of Paper V and extend it with the rates-based description of dust formation in an oxygen-rich chemistry. Specifically, we here focus on a wind where only forsterite is formed. To enable this study, we calculated new gas opacity tables for solar metallicities based on the EXOMOL

database (Tennyson et al. 2020), and also added free-free and bound-free opacities calculated using the JEKYLL code (Ergon et al. 2018; Ergon & Fransson 2022). We are thereby, for the first time, able to study time-dependent models using high spatial resolution in an oxygen-rich chemistry that include drift.

We first make semi-analytical predictions of the drift velocity in Sect. 2 to see what we can deduce based on simple physical arguments. Thereafter, we describe the physics features of our physically enhanced models in Sect. 3. Presentations of the modelling procedure and results follow in Sect. 4. We discuss the influence of drift on our results in Sect. 5 and close the paper with our conclusions in Sect. 6.

2. Semi-analytic predictions of drift

Before we engage in numerical and physical details of our updated version of T-800, we look at a simplified treatment of the oxygen-rich stellar-wind formation problem to estimate what the associated drift velocities could be. We address the balancing forces that give rise to the wind in Sect. 2.1. Thereafter we, anew, look at the concept of complete momentum coupling in Sect. 2.2 and conclude this analysis in Sect. 2.3.

2.1. Balancing dust extinction and radiation pressure

To estimate the drift velocity for a given set of stellar parameters, we need to estimate the radiation pressure on the dust component. Thus, we need to know the photon-to-dust grain momentum transfer efficiency. Absorption and scattering of photons by dust grains is modelled with the effective cross sections $\sigma_{\text{abs},\nu}$ and $\sigma_{\text{sca},\nu}$, where ν is the frequency. The efficiency of absorption and scattering, or the combination of the two (extinction), is usually defined relative to the geometric cross section σ . For spherical grains, $\sigma = \pi a^2$, where a is the grain radius. The absorption efficiency $Q_{\text{abs},\nu} = \sigma_{\text{abs},\nu}/\sigma$ is related to the extinction and scattering efficiencies $Q_{\text{ext},\nu} = \sigma_{\text{ext},\nu}/\sigma$ and $Q_{\text{sca},\nu} = \sigma_{\text{sca},\nu}/\sigma$, as

$$Q_{\text{abs},\nu} = Q_{\text{ext},\nu} - Q_{\text{sca},\nu}. \quad (1)$$

To calculate a correct radiation pressure, it is necessary to use the absorption efficiency (we name this term $Q_{\text{abs},\nu}(\text{pr})$ in Paper V),

$$Q_{\text{rp},\nu} = Q_{\text{ext},\nu} - g_{\text{sca},\nu} Q_{\text{sca},\nu} = Q_{\text{abs},\nu} - (g_{\text{sca},\nu} - 1) Q_{\text{sca},\nu}, \quad (2)$$

where $g_{\text{sca},\nu} = \langle \cos \theta \rangle_{\nu}$ is the average scattering angle. Mie theory (Bohren & Huffman 1983) provides these efficiencies as well as the average scattering angle.

In many extant works on AGB winds (e.g., Sandin & Höfner 2003; Mattsson et al. 2008, 2010), the radiation pressure is calculated assuming dust grains are small compared to the wavelength of the incident radiation. This, so called, small-particle limit (SPL) approximation leads to the simplification $Q_{\text{ext},\nu} = Q'_{\nu}/a$, where Q'_{ν} is a function of only the frequency (Wickramasinghe 1972). Figure 1 shows how $Q_{\text{rp},\nu}$, as computed based on Mie theory, compares to the corresponding SPL value of $Q_{\text{ext},\nu}$, using optical constants of (Jäger et al. 2003). An important feature is the [blue] “peacock feather” region where the Mie-theory based radiation force on grains of radius a in an optically thin atmosphere is (where the Eddington flux $H_{\nu}(r) \approx 0.25(R_{\star}/r)^2$),

$$f_{\text{rad,d}} = \frac{\pi}{c} \left(\frac{R_{\star}}{r} \right)^2 n_{\text{d}}(a) \int_0^{\infty} a^2 Q_{\text{rp},\nu}(a) B_{\nu}(T_{\text{eff}}) d\nu, \quad (3)$$

where R_{\star} is the stellar radius, n_{d} the grain number density, and B_{ν} the Planck function. Grain sizes in the region of relevant val-

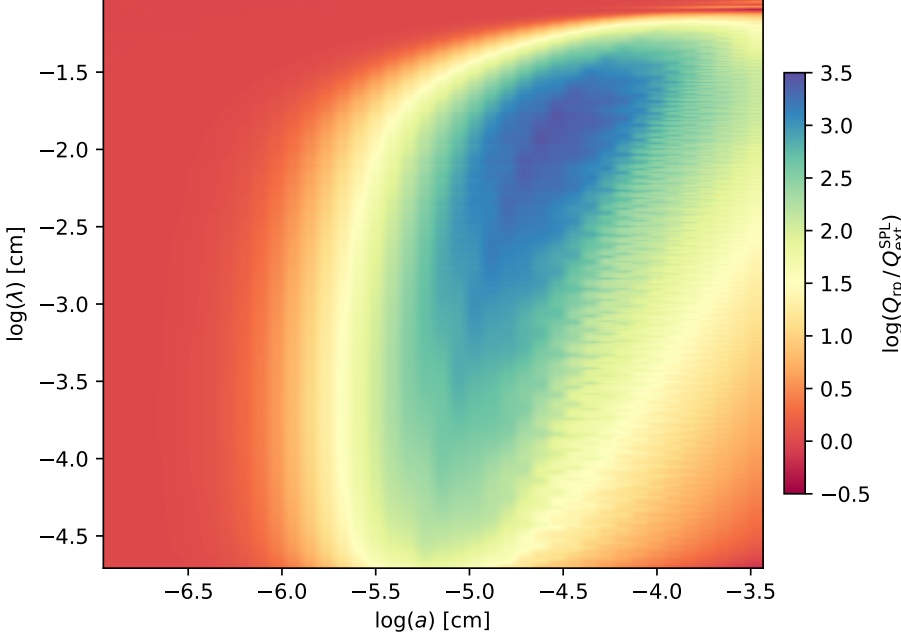


Fig. 1. Ratio of the radiation pressure efficiency $Q_{rp,v}$ to the SPL extinction efficiency versus the grain radius and wavelength, assuming spherical forsterite grains.

ues ($0.1 \lesssim a \lesssim 0.5 \mu\text{m}$) result in a radiation pressure about 300–30 times lower in the spectral region near the typical flux peak of M-type AGB stars ($\lambda \simeq 1 \mu\text{m}$) when the SPL is assumed.

2.2. Momentum coupling and equilibrium drift

The fraction of the momentum that is transferred from the radiation field to the gas is referred to as the level of momentum coupling. In Paper V, complete momentum coupling (CMC) was defined as the case of force balance between radiation on the one hand and drag and gravity on the other, although the amount of momentum lost owing to the gravitational potential is negligible. Equating radiation and drag force is also a common definition of CMC.

Drift is a non-linear dynamic phenomenon, but simulations (in particular those of Paper V) show that an equilibrium tends to develop in most cases. Equilibrium drift can be defined as the situation where the Lagrangian derivatives of gas and dust velocity are equal, i.e., $dv/dt = du/dt$. This, in turn, means that the equilibrium drift velocity \dot{v}_D is constant with respect to time and that \dot{v}_D is governed by a simple algebraic equation instead of a hard-to-solve partial differential equation.

Assuming equilibrium drift and CMC defined as above, the drag force is $f_{\text{drag}} = f_{\text{rad,d}} - f_{\text{grav,d}}$. Defining the dimensionless variable

$$S_D = \frac{\dot{v}_D}{v_\zeta}, \quad \text{and} \quad v_\zeta = \sqrt{\zeta T_g} = \sqrt{\frac{128k_B}{9\pi\mu m_H} T_g},$$

where v_ζ is a modified thermal velocity, k_B is the Boltzmann constant, μ the mean molecular weight, m_H the mass of a hydrogen atom, and T_g the gas temperature. We then have

$$S_D^2 = -\frac{1}{2} + \left\{ \frac{1}{4} + \left(\frac{f_{\text{rad,d}} - f_{\text{grav,d}}}{f_\zeta} \right)^2 \right\}^{\frac{1}{2}}. \quad (4)$$

where $f_{\text{grav,d}} \approx \rho_d GM_\star r^{-2}$ is the point-mass approximation for the gravitational force, ρ_d the dust density, G the Gravitational constant, and $f_\zeta = \pi a^2 n_d \rho_g v_\zeta^2$ can be seen as a thermal coupling

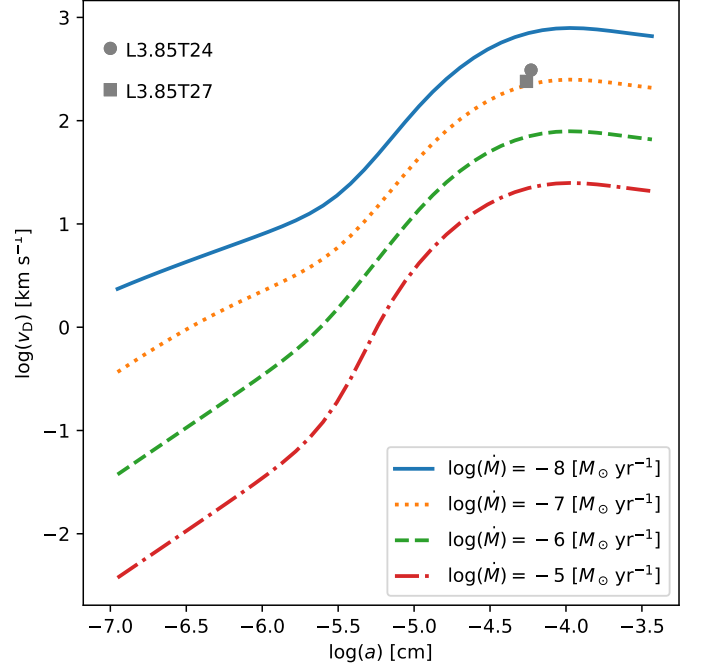


Fig. 2. Equilibrium drift velocity \dot{v}_D versus grain radius, assuming CMC. Four lines show different wind densities (mass-loss rates) as explained in the legend. The grey bullet and square indicate the locations of the two numerical simulations with drift presented in Sect. 4.3.

force between gas and dust; and here, ρ_g is the gas density. For a given mass-loss rate \dot{M} , wind expansion velocity u_∞ , luminosity L_\star , effective temperature T_{eff} , and stellar mass M_\star , we can now estimate the equilibrium drift velocity \dot{v}_D using the above equation in combination with the condition for mass conservation $\dot{M} = 4\pi r^2 \rho_g u_\infty$ and $L_\star = 4\pi \sigma_{\text{SB}} R_\star^2 T_{\text{eff}}^4$, where σ_{SB} is the Stefan-Boltzmann constant.

2.2.1. Predicted drift velocities

In Fig. 2 we show the expected equilibrium drift velocity \dot{v}_D versus grain radius a for $M_\star = 1 M_\odot$, $\log(L_\star) = 3.85 L_\odot$, $T_{\text{eff}} = 2700$ K and four different assumptions of mass-loss rates, chosen to represent the range of mass-loss rates predicted by models (B19) and observations (see, e.g., Uttenthaler et al. 2019, and references therein). We note that there is ample room for high drift velocities and that the maximum drift velocity of each curve occurs for grain radii that are quite typical for M-type AGB stars according to extant models (B19).

It is clear that a wind driven by radiation pressure on forsterite grains leads to high drift velocities, even in case of massive outflows. It has been argued that drift is negligible in winds associated with very high mass-loss rates (Höfner & Olofsson 2018), which seems to be the case for carbon stars (see Fig. 3a in Paper V); however, our more recent model of the stellar wind in IRC+10°216 says otherwise (see Fig. 8 in Andersson et al. 2022). But given that M-type AGB stars have wind speeds of $u_\infty \sim 10 \text{ km s}^{-1}$ and typical grain sizes $a \simeq 0.5 \mu\text{m}$, the drift factor $\mathfrak{F}_D = 1 + v_D/u_\infty > 2$ also for intense outflows. ($\mathfrak{F}_D > 2$ corresponds to a situation where the drift velocity v_D exceeds the gas expansion velocity u_∞ and the dust mass-loss rate is typically reduced by an order of magnitude or more.) We tentatively conclude that including drift in the modelling of M-type AGB stars is of absolute fundamental importance, as PC models do not provide a correct result even in the high-mass-loss limit. As we shall see, this conclusion is also confirmed by our detailed modelling, described below.

2.3. Physical interpretation of the PC assumption

The PC assumption is incompatible with the idea that AGB winds form by friction between radiatively accelerated dust grains and gas particles. MS21 argue that there is no realistic physical limiting case which leads to PC. Whilst this must still be true, we shall here discuss the (unrealistic) limit where PC is formally true.

Considering Eq. (4), we note that $(f_{\text{rad,d}} - f_{\text{grav,d}})/f_\zeta \ll 1$ implies $S_D = 0$, i.e., no drift. If we ignore the case $f_{\text{rad,d}} = f_{\text{grav,d}}$, this limit requires that f_ζ is very large and, in particular, much larger than the net radiation force $\tilde{f}_{\text{rad,d}} = f_{\text{rad,d}} - f_{\text{grav,d}}$. For this to occur in the case given in the previous section (with $f_{\text{rad,d}}$ obtained from Eq. (3)), the modified thermal velocity v_ζ has to be of the order 100 km s^{-1} unless ρ_g is several orders of magnitude higher than expected in a realistic wind. Such a high v_ζ corresponds to gas temperatures of the order 10^5 K, which is completely unrealistic. It is, in fact, fair to say that the physical interpretation (or consequence) of the assumption of PC is quite absurd. The semi-analytic predictions of drift velocity presented here provide a solid theoretically founded reason for pursuing detailed modelling of winds of M-type AGB stars with gas and dust treated as dynamically decoupled phases.

3. Model features and improvements of T-800

The model features of our radiation hydrodynamic model code T-800 is described in Paper V. As in the C-rich chemistry, we model three components in the O-rich chemistry described here: the gas, the radiation field, and a dust component consisting of forsterite (Fo) mineral grains.

In comparison to the moments method used to describe dust formation in the C-rich chemistry, we replace the four dust moment equations (K_0 – K_3) with one rate equation for the forma-

tion of each mineral k , and the carbon number density equation (Eq. (5) in Paper V) with corresponding equations for each affected tracer element j . All physics of mineral formation in oxygen-rich chemistry we require is developed and described by Gail & Sedlmayr (1999) and GS14. The adjusted equations are

$$\frac{\partial}{\partial t} n_{d,k} N_k + \nabla \cdot (n_{d,k} N_k v_k) = q_k, \quad (5)$$

$$\frac{\partial}{\partial t} n_j + \nabla \cdot (n_j u) = -v_k^j q_k, \quad (6)$$

where t is the time, $n_{d,k}$ the seed particle density, N_k the number of monomers, v_k the mean dust particle velocity, q_k the sum of the source and sink terms owing to grain formation, n_j the tracer element atom number density, v_k^j the number of tracer element atoms per monomer, and u the gas velocity. In this approach, there is no description of nucleation. Instead, seed particles of species are assumed to exist everywhere and

$$n_{d,k} = \rho_g \frac{\epsilon_k}{m_u \mu}, \quad (7)$$

where ρ_g is the gas density, ϵ_k the seed particle abundance, m_u the atomic mass constant, and $\mu = 1.26$ the mean molecular weight.

3.1. The mineral rate equation

The rate equations describe the number of monomers N_k throughout the model domain. The rate equation source term owing to grain growth, evaporation, and destruction is

$$q_k = n_{d,k} \left[4\pi a_k^2 (J_{\text{gr},k} - J_{\text{ev},k}) - \frac{1}{\tau_{\text{sp,n}}^k} \right], \quad (8)$$

where a_k is the particle radius, J_{gr} (J_{ev}) the growth (evaporation) rate, and $1/\tau_{\text{sp,n}}$ the rate of non-thermal sputtering. The grain radius is described using the grain volume V and the monomer volume V_1 ,

$$a_k = \left(\frac{3V_k}{4\pi} \right)^{\frac{1}{3}}, \quad V_k = N_k V_{1,k}, \quad V_{1,k} = \frac{\mathcal{A}_k m_u}{\rho_{m,k}}, \quad (9)$$

where \mathcal{A}_k is the molecular weight and $\rho_{m,k}$ the mineral intrinsic density.

The term that describes grain growth and evaporation is written as (GS14, Eqs. 12.101, 12.102, and 12.108)

$$J_{\text{gr},k} - J_{\text{ev},k} = \xi_k \frac{p_j}{\sqrt{2\pi m_j k_B T_g}} \left(\phi_k - \frac{1}{a_k^\epsilon} \sqrt{\frac{T_g}{T_d}} \right), \quad (10)$$

where ξ_k is the the drift-velocity-dependent sticking coefficient, p_j and m_j are the partial pressure and mass of the rates-determining component, respectively. Moreover, k_B is Boltzmann's constant, T_g the gas temperature, ϕ_k the drift correction factor, a_k^ϵ the reaction activity, and T_d the dust temperature.

The sticking coefficient¹ ξ_k is assumed to decrease when the drift velocity becomes high in relation to the binding energy $E_{b,k}$ (Eq. (14) in Krüger & Sedlmayr 1997 and Eq. (13) in Sandin & Höfner 2004, hereafter Paper III).

$$\xi_k = \xi^{(k)} \exp \left[- \left(\frac{\mathcal{A}_k m_u \tilde{w}_k^2}{8E_{b,k}} \right)^3 \right], \quad (11)$$

¹ Please note that in MS21 ξ was used to denote the grain-growth velocity, which is a different, although not unrelated, quantity.

where the velocity of dust grains relative to gas particles \tilde{w}_k is (Eqs. 11 and 12 in Paper III)

$$\tilde{w}_k = \left(\frac{8k_B T_g}{16\pi \mathcal{A}_k m_u} + \frac{v_{D,k}^2}{16} \right)^{\frac{1}{2}}. \quad (12)$$

Here, $v_{D,k} = v_k - u$ is the drift velocity. Moreover, the drift correction factor ϕ_k is (Eq. (12.19) in GS14)

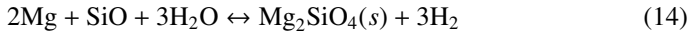
$$\phi_k = \left(1 + \frac{\pi \mathcal{A}_k m_u}{8k_B} \frac{v_{D,k}^2}{T_g} \right)^{\frac{1}{2}}. \quad (13)$$

We use the same expression for non-thermal sputtering ($1/\tau_{sp,n}^k$) as we do in Paper III. Although, here we account for collisions with H_2 molecules, in addition to H and He atoms.

3.2. Growth and evaporation of forsterite

We use two tracer elements: silicon and magnesium. There are in this case eleven equations, instead of thirteen equations when using the moments approach and a carbon-rich chemistry. Forsterite grain growth takes place through collisions of seed grains and extant grains with either SiO molecules or Mg atoms; when addition of SiO (Mg) is the rate determining reaction step, $p_j = p_{SiO}$ and $m_j = m_{SiO}$ ($p_j = p_{Mg}$ and $m_j = m_{Mg}$).

The basic chemical reaction for the forsterite formation, as well as its evaporation through chemical sputtering, is



and the (chemical sputtering) reaction activity a_{Fo}^c is (see Eqs. 12.60, 12.103, and 12.104 in GS14)

$$\frac{1}{a_{Fo}^c} = \frac{p_{H_2}^3}{p_{SiO} p_{Mg}^2 p_{H_2O}^3} \frac{K_p(SiO) K_p^3(H_2O)}{K_p(Mg_2SiO_4) K_p^3(H_2)}, \quad (15)$$

where the four equilibrium constants K_p are calculated at the dust temperature T_d .

3.3. Partial pressures of atoms and molecules

The number densities of the molecules in the gas phase that are part of the grain formation as well as the activities that determine when dust grains form are calculated in an equilibrium chemistry of molecules with hydrogen, oxygen, carbon, nitrogen, aluminium, silicon, and sulfur, following the approach of GS14 (chapter 10.3). The considered atoms and molecules are: H, H_2 , O, OH, H_2O , CO, CO_2 , CH_4 , N, N_2 , NH_3 , HCN, Al, AlO, AlS, AlOH, AlO₂H, Al₂O, Al₂O₂, Si, SiO, SiO₂, S, SO, HS, H_2S , SiS, and S₂. Magnesium is assumed to be present as free atoms.

All number densities and activities are calculated for the temperature range $100 \leq T_g \leq 10000$ K. We use equilibrium constants K_p – that are often referred to as dissociation constants – of Sharp & Huebner (1990), GS14 (see their Table A.5), and NIST JANAF².

4. Modelling procedure and results

We first briefly point at our modelling procedure in Sect. 4.1 and then describe the physics setup and choice of model parameter sets in Sect. 4.2. We present our results in Sect. 4.3.

² Equilibrium-constant data of NIST/JANAF can be retrieved from <https://janaf.nist.gov/>

Table 1. References of used atom and molecule datasets as well as number of energy levels accounted for in each entry.

molecule	dataset	References	Energy levels
C	Kurucz	1	999
C ₂	8states	2, 3	44 189
C ₂ H ₂	aCeTY	4	5 160 803
CH	MoLLIST	5, 6	2526
CH ₄	YT34to10	7, 8	8 194 057
CN	Trihybrid	9, 10, 11	7703
CO	Li2015	12, 13	6383
CO ₂	UCL-4000	14	3 562 798
CS	JnK	15	11497
CrH	MoLLIST	6	1646
FeH	MoLLIST	16, 6	3564
H ₂	RACPPK	17	302
H ₂ O	POKAZATEL	18	810 269
H ₂ S	AYT2	19	220 618
HCl	HITRAN	20	335
HCN	Harris	21, 22	168 110
HF	Coxon-Hajig	23, 24, 13	684
LaO	BDL	25	38 208
MgH	XAB	26	1303
N	Kurucz	1	283
N ₂	WCCRMT	27, 28, 29	40 380
NH ₃	CoYuTe	30, 31	5 095 730
O	Kurucz	1	201
OH	MoLLIST	32, 33, 6	1878
SO ₂	ExoAmes	34	3 270 270
SiO	SiOUVenIR	35	174 250
SiS	UCTY	36	10 104
TiO	Toto	37	236 308
VO	VOMYT	38	638 958
YO	SSYT	39	79 440

References. (1) Kurucz & Bell (1995); (2) Yurchenko et al. (2018b); (3) McKemmish et al. (2020); (4) Chubb et al. (2020); (5) Masseron et al. (2014); (6) Bernath (2020); (7) Yurchenko & Tennyson (2014); (8) Yurchenko et al. (2017); (9) Brooke et al. (2014); (10) Syme & McKemmish (2020); (11) Syme & McKemmish (2021); (12) Li et al. (2015); (13) Somogyi et al. (2021); (14) Yurchenko et al. (2020); (15) Paulose et al. (2015); (16) Dulick et al. (2003); (17) Roueff et al. (2019); (18) Polyansky et al. (2018); (19) Azzam et al. (2016); (20) Gordon et al. (2017); (21) Harris et al. (2006); (22) Barber et al. (2014); (23) Li et al. (2013); (24) Coxon & Hajigeorgiou (2015); (25) Bernath et al. (2022); (26) Owens et al. (2022); (27) Western et al. (2018); (28) Western (2017); (29) Shemansky (1969); (30) Al Derzi et al. (2015); (31) Coles et al. (2019); (32) Brooke et al. (2016); (33) Yousefi et al. (2018); (34) Underwood et al. (2016); (35) Yurchenko et al. (2022); (36) Upadhyay et al. (2018); (37) McKemmish et al. (2019); (38) McKemmish et al. (2016); (39) Smirnov et al. (2019)

4.1. Modelling procedure

We follow the modelling procedure described in Sect. 3.1 in Paper V. Due to the low outflow velocity of the wind ($u_\infty \lesssim 10$ km s⁻¹), we set the outer boundary here at $r_{\text{final}}^{\text{ext}} = 20R_\star$. We use $N_d = 840$ grid points, which very nearly corresponds to the grid point arrangement we achieve when using $N_d = 1024$ and $r_{\text{final}}^{\text{ext}} = 40R_\star$. It appears to be sufficient to evolve the wind models for a time interval of about $100P$ (stellar pulsation periods) as the wind structures reach a state of equilibrium before that.

4.2. Physics setup and selection of model parameters

We introduce effects of gas-to-dust drift using one mean dust velocity. We compare the new drift models to PC (non-drift) models that are in all other ways equivalent to the drift models.

We used solar abundances of Anders & Grevesse (1989), with values for C and O of Grevesse & Sauval (1994). As do B19, we set the pulsation period (P) using the P – L_* -relation of Whitelock et al. (2009). To correct for too small bolometric variations (Gautschi-Loidl et al. 2004), B19 (see their Sect. 2.2) introduce a free parameter f_L that allows larger variations of the luminosity at the inner boundary. Whilst we added the option to T-800 to use a freely chosen value on f_L , we use $f_L = 1$ here as we do not calculate model spectra and results of a PC model using both approaches are indistinguishable.

Next, we describe our approach to calculate gas opacities in Sect. 4.2.1, dust properties in Sect. 4.2.2, and our selection of model parameters in Sect. 4.2.3.

4.2.1. Gas opacities

In Paper V, we used tabulated gas opacities $\kappa_v(\rho_g, T_g)$ that were created for carbon-rich chemistries with the COMA code (Aringer 2000; Aringer et al. 2009) for 319 wavenumbers in the interval $400 \leq \tilde{\nu} \leq 39\,480 \text{ cm}^{-1}$, 50 temperatures in the interval $1000 \leq T_g \leq 10\,000 \text{ K}$, and 24 densities in the interval $-18 \leq \log_{10} \rho_g \leq -6 \text{ g cm}^{-3}$.

Here, we calculated new bound-bound gas opacities based on data of the EXOMOL project (Tennyson et al. 2020).³ The calculations make use of data for the following 30 atoms and molecules: C, C₂, C₂H₂, CH, CH₄, CN, CO, CO₂, CS, CrH, FeH, H₂, H₂O, H₂S, HCl, HCN, HF, LaO, MgH, N, N₂, NH₃, O, OH, SO₂, SiO, SiS, TiO, VO, and YO, see Table 1. The number of energy levels for each dataset is specified here, however the corresponding number of transitions, or lines, is typically at least an order of magnitude larger. For example, the ExoMol aCeTY C₂H₂ line list has around 5.2 million energy levels and 4.3 billion transitions (Chubb et al. 2021). We used EXOCROSS (Yurchenko et al. 2018a) to calculate cross sections σ_l for each atom and molecule l at $102\,750$ wavenumbers in the interval $100 \leq \tilde{\nu} \leq 41\,200 \text{ cm}^{-1}$, 105 temperatures in the interval $100 \leq T_g \leq 10\,000 \text{ K}$, and 24 gas densities in the interval $-18 \leq \log_{10} \rho_g \leq -6 \text{ g cm}^{-3}$. The cross sections are resampled to a coarse grid of a pre-defined set of wavenumbers, where the resulting cross section is the average of the ten nearest cross sections on the finer grid. Currently, we used 384 wavenumbers; this is an even multiple of the number of cores available on each node (2×64) on a current high-performance cluster we used. Individual cross sections are thereafter converted to bound-bound opacities by multiplying with the corresponding partial pressure p_l as

$$\kappa_{\text{bb},l} = \frac{p_l}{k_B T_g} \frac{\sigma_l}{\rho_g} \left[\text{cm}^2 \text{g}^{-1} \right]. \quad (16)$$

We calculated partial pressures for the 27 molecules listed above as well as the three individual atoms using the same approach as in Sect. 3.3.

Bound-bound opacities become low at higher temperatures ($T_g \gtrsim 2000 \text{ K}$), where instead bound-free opacities κ_{bf} and free-free opacities κ_{ff} dominate. We calculated such opacities using the JEKYLL code (Ergon et al. 2018; Ergon & Fransson 2022), see Appendix A for more information. Free-free opacities $\kappa_{\text{ff},i}$ were calculated for each ion i separately using an expression that

³ <https://www.exomol.com/>

Table 2. Dust parameters: forsterite

parameter	value	B19 ^a	unit	Reference
ϵ_{Fo}	10^{-15}	10^{-15}		1
\mathcal{A}_{Fo}	140.694	140		2, 3
$\rho_{\text{m,Fo}}$	3.21	3.27	g cm^{-3}	2, 3
ξ_{Fo}	0.1	1.0		4
$E_{\text{b,Fo}}$	3.5	–	eV	5
$\nu_{\text{Fo}}^{\text{Si}}, \nu_{\text{Fo}}^{\text{Mg}}$	1, 2 ^b	1, –		

References. (1) B19; (2) Lide (1995); (3) GS14, Table 12.1; (4) GS14, Sect. 12.7.1; (5) Barlow (1978), the ‘‘Silicate’’ entry in Table 4

Notes.^a The values we assume B19 use are specified by Höfner et al. (2016). ^b For all elements j , but Mg and Si, $\nu_{\text{Fo}}^j = 0$.

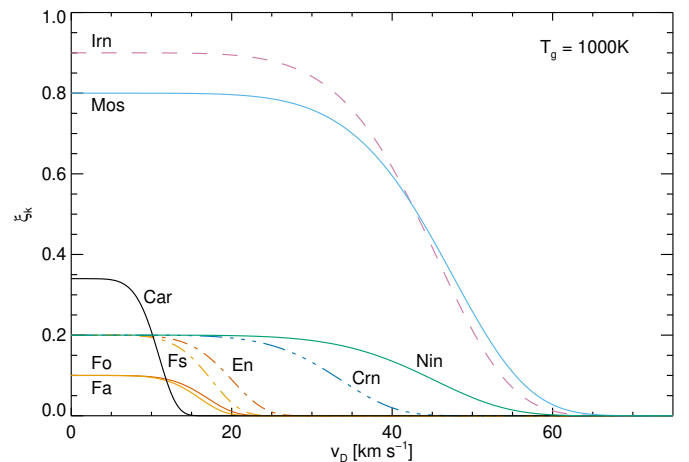


Fig. 3. The sticking coefficient ξ_k (Eq. (11)) versus the drift velocity v_D for nine different minerals, assuming a gas temperature $T_g = 1000 \text{ K}$.

depends on provided electron and ion densities (e.g. Eq. (5.149) in Hubeny & Mihalas 2015).

Finally, bound-bound and bound-free opacities of individual atoms, molecules, and ions and free-free opacities of ions are summed up to provide a total abundances-dependent gas opacity for each pair of gas density and gas temperature,

$$\kappa_v(\rho_g, T_g) = \sum_l \kappa_{\text{bb},l} + \sum_i (\kappa_{\text{bf},i} + \kappa_{\text{ff},i}).$$

Each set of abundances-specific opacities are saved in a binary file tabulated in wavenumber, density, and temperature. The opacities are interpolated in density and temperature for each individual wavenumber in the radiative transfer calculations using two-dimensional rational splines (Späth 1995).

We were at first kindly provided with the same opacity table for solar metallicities that B19 use (Aringer, priv. comm.). Due to unknown reasons, we were unsuccessful in using these data with our new models. We discuss these extant opacity data and make a simple comparison with our new opacities in Appendix B.

4.2.2. Dust properties

We list all forsterite-specific dust parameters we used in Table 2. We illustrate how the sticking coefficient ξ_k varies with the drift velocity for forsterite and eight other minerals in Fig. 3 (cf. Fig. 1 in Paper III); the parameters of the eight additional minerals are taken from the same set of references as for forsterite, noting that

condensation is (cf. Eq. (12.85) in GS14)

$$\tilde{f}_{\text{cond}}^j = \frac{1}{\varepsilon_j} \sum_k N_k \epsilon_k v_k^j. \quad (18)$$

Moreover, the dust-to-mass mass-loss ratio is

$$\frac{\dot{M}_d}{\dot{M}} = \sum_k \frac{\rho_{d,k}}{\rho_g} \frac{v_{\infty,k}}{u_{\infty}} = \sum_k \delta_{dg,k} \tilde{\delta}_{D,k}, \quad (19)$$

where $\delta_{dg,k} = \rho_{d,k}/\rho_g$.

We calculated a relative fluctuation amplitude \hat{r} for each property Q as $\hat{r} = \sigma_s/Q$, where σ_s is the (sample) standard deviation of the property Q in the time interval that is used to measure the same property. We show results of our model calculations in Table 4.

5. Discussion

We analyze the new results of our PC models in Sect. 5.1 and then compare PC models with our new drift models in Sect. 5.2.

5.1. Comparing results of the PC (non-drift) models

5.1.1. The lower temperature model L3.85T24

Our PC models using a unity sticking coefficient ($\xi^{(Fo)} = 1.0$) reveal a more massive wind than when $\xi^{(Fo)} = 0.1$. The mass-loss rate and expansion velocity are 6.5 and 3.0 times higher, respectively. A lower ratio of 2.2 is seen in the degree of condensation and the dust-to-gas density ratio. The average grain radius is only 30 % higher. The fluctuation amplitudes are 26–40 times higher in all values, but the mass-loss rate, where it is 130 times higher. Clearly, a unity sticking coefficient results in a much more variable wind where all values but the grain radius are drastically higher, but the increase is with the exception of the mass-loss rate 30–200 % and not a factor 10.

In comparison to B19, and assuming a unity sticking coefficient, our values on the degrees of condensation and dust-to-gas density ratio are 51–58 % higher, the grain radius 15 % higher and the mass-loss rate 30% lower. These values compare fairly well.

5.1.2. The proof-of-concept model L3.85T27

H08 presents model L3.85T27 (“model B”) as a proof of the concept that scattering on larger dust particles in place of absorption allows formation of massive stellar winds in M stars. B19 calculate a model with the same stellar parameters, also with 100 grid points, but use a somewhat longer pulsation period ($P = 478$ d, instead of $P = 390$ d) and also favor a lower pulsation amplitude ($\Delta u_p = 2$ km s⁻¹). We used the same stellar parameters as B19, where $\Delta u_p = 4$ km s⁻¹. We also set the sticking coefficient to unity, but we used a higher spatial resolution achieved with $N_D = 840$ grid points. We show the resulting values of both H08 and B19 in Table 4 for easy reference.

Notably, our new values on the silicon degree of condensation and the mean grain radius agree well with these two studies; our values are 83 % and 94 % of their values, respectively. Similarly, our value on the dust-to-gas ratio is 85 % of the value of B19. Regarding the mass-loss rate and expansion velocity, our values are 25 % and 67 % (4.7 % and 51 %) of the values of H08 (B19). Our mass-loss rate is, obviously, closer to the value of H08, whilst the difference is much larger in comparison to B19.

5.2. Comparing results of the drift models

5.2.1. Effects of the sticking coefficient

The drift model shows a different result in comparison to the PC model L3.85T24 – the values of the two drift models are similar (they differ by 5.6–33 %), with the exception of the mass-loss rate where the value of the unity sticking coefficient model is 6.0 % of the other model. Thus, the model with the lower sticking coefficient results in a much higher mass loss. Plausibly, because less efficiently formed dust grains can flow to regions where they more effectively contribute to wind formation, before there is enough dust to accelerate both the dust and gas outwards. The fluctuation amplitudes are, moreover, all very similar (they differ by 0–48 %). Notably, the very high drift velocity of 240 km s⁻¹ increases by 29% to 310 km s⁻¹ in the unity model. The true degrees of condensation are a factor twenty lower than the modified degrees of condensation owing to the high drift velocities.

We compare the drift model using $\xi^{(Fo)} = 0.1$ with our PC model where $\xi^{(Fo)} = 1.0$. The mass-loss rate of the drift model is 86 % lower, the dust-to-gas density ratio 22 times higher, and the true degrees of condensation 95 % lower than the corresponding values of the PC model. The differences are much smaller in the expansion velocity (17 % lower) and the grain radius (0.73 % higher). The same comparison with the model of B19 gives a 90 % lower mass-loss rate, a 35 times higher dust-to-gas density ratio, and a 92 % lower degree of condensation of silicon. Similarly, differences are smaller in the expansion velocity (26 % lower) and the grain radius (15 % higher). The huge increase in the dust-to-gas density ratio of the drift model must be put in context of the drastically lower mass-loss rate. Nevertheless, the differences in comparison to the PC models of about a factor ten in the mass-loss rate and a factor 35 in the dust-to-gas density ratio are large and must not be ignored.

5.2.2. The proof-of-concept drift model L3.85T27

The values of the drift model again differ from our PC model. The mass-loss rate is here 95 % lower, the dust-to-gas density ratio 82 times higher, and the degrees of condensation 92 % lower. Furthermore, the expansion velocity is 160 % higher, and the mean grain radius 32 % higher. Temporal fluctuations are higher in the dusty properties, but the fluctuations are generally low. Both the drift model and the PC model show periodic variations. The mass-loss rate is 0.24 % of the value of B19, the dust-to-gas density ratio 70 times higher, and the degree of condensation of silicon 93 % lower. The expansion velocity is 29 % higher and the grain radius 25 % higher.

We plot our PC and drift models versus the radius in Fig. 4. The inefficient mass loss of the drift model is seen in the gas density that is a hundred times lower than in the PC model (Fig. 4b). Despite the lower mass-loss rate, the expansion velocity of the drift model is more than twice as high than in the PC model, see Fig. 4a. The gas opacity κ_H increases somewhat towards higher radii (Fig. 4j), whilst the Rosseland mean opacity κ_R decreases to be a millionth and less of κ_H at higher radii; notably, the same ratio is closer to a factor ten in the carbon-rich model shown in Fig. 8j in Paper V. The Eddington factor of both models (Fig. 4g) indicates that there is no need to solve the equation of radiative transfer where $R \gtrsim 10 R_*$, as the factor is very close to unity.

The drift velocity shown in Fig. 4c attains high values already near the star. The same high values cause an abrupt cut-off in the dust formation rates at radii $r \lesssim 3 R_*$ (Fig. 4e). The

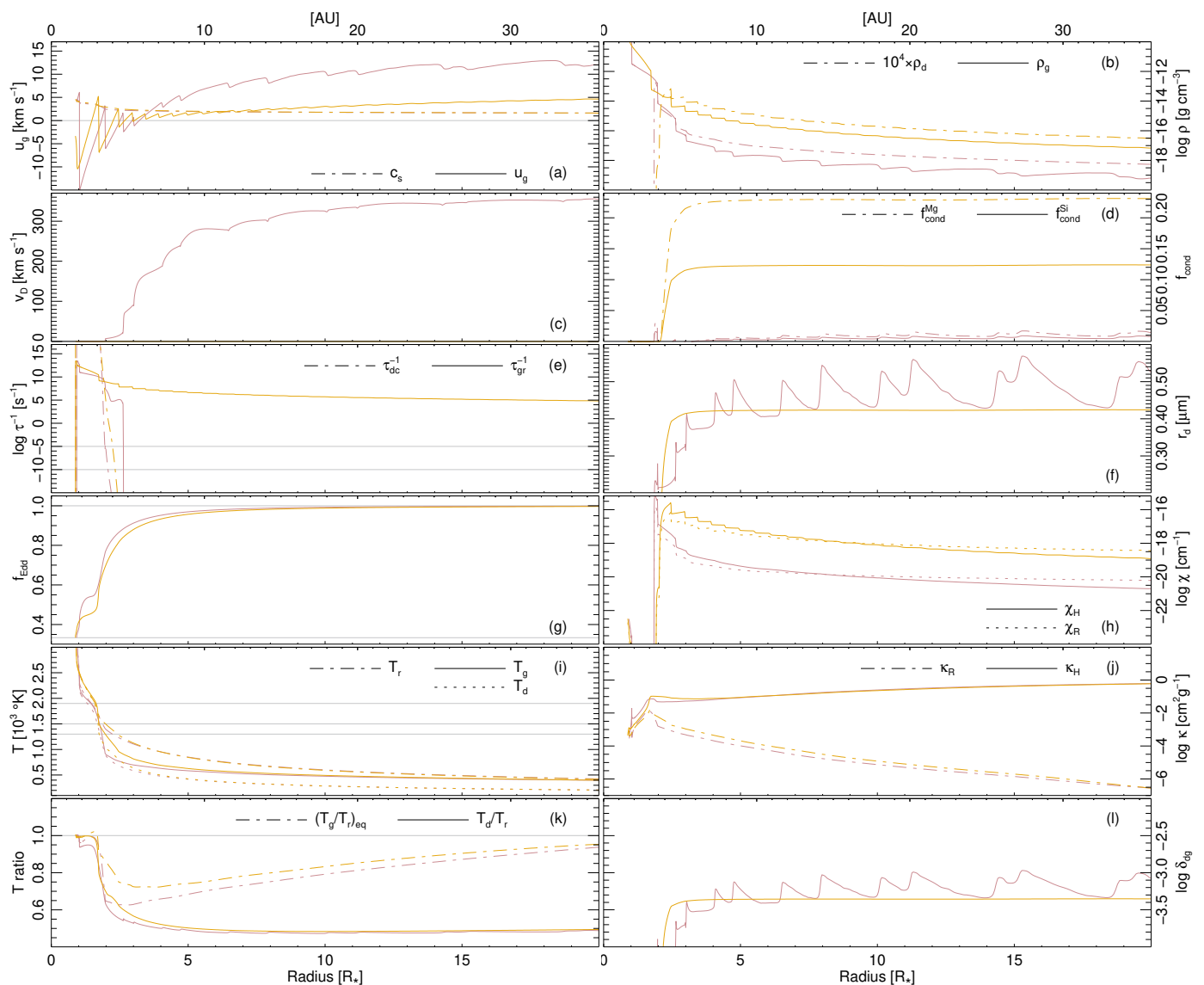


Fig. 4. Radial structure of a snapshot of setup L3.85T27 for the full modelled region. The drift model (where $\xi^{(\text{Fo})} = 0.1$; PC model, where $\xi^{(\text{Fo})} = 1.0$) is shown with purple (orange) lines. From the top left, the 12 panels show: (a) gas velocity u_g , sound speed c_s ; (b) gas density ρ_g , dust density $10^4 \times \rho_d$ (log); (c) drift velocity v_D ; (d) [true] degree of condensation of silicon $f_{\text{cond}}^{(\text{Si})}$ and magnesium $f_{\text{cond}}^{(\text{Mg})}$; (e) net growth rate τ_{gr}^{-1} , net decay rate τ_{dc}^{-1} (log); (f) average grain radius r_d ; (g) Eddington factor f_{Edd} ; (h) extinction coefficient χ_{H} , Rosseland mean extinction coefficient χ_{R} ; (i) gas temperature T_g , radiative temperature T_r , and dust temperature T_d ; (j) gas opacity κ_{H} and Rosseland mean opacity κ_{R} (log); (k) temperature ratios T_d/T_r and $(T_g/T_r)_{\text{eq}}$; and (l) dust-to-gas density ratio δ_{dg} . All properties are drawn versus the stellar radius R_* (lower axis) and astronomical units (AU; upper axis). Grey horizontal lines are guides.

[true] degree of condensation (Fig. 4d) and extinction coefficient (Fig. 4h) are significantly lower in the drift model.

The dust-to-radiative temperature ratio in Fig. 4k shows a value that is the inverse of the same ratio in a stellar wind of a carbon star (cf. Fig. 8k in Paper V). The forsterite dust temperature is always lower than the radiative temperature; it is about half as high in the outer regions. In comparison, the amorphous carbon dust temperature is always higher than the radiative temperature; and it is up to about 50% higher in the outer regions. No other indicator illustrates the difference as clearly between scattering and absorption dominated dust extinction.

5.2.3. Implications of allowing gas-to-dust drift

The differences between the two drift models and the corresponding PC models are enormous. Our values on the mass-loss rates of the PC models are 7.5 and 21 times higher than the corresponding drift model. These values grow to 11 and 420 times when we instead compare with the corresponding values of B19. And the mass-loss rate of the proof-of-concept model of H08 is 93 times higher than in our drift model. Besides different model parameters and modeling approach, the differences are owing to the scattering-dominated dust extinction of forsterite, which results in extraordinarily high drift velocities. Such high drift velocities imply that any features in the diluted dust component in observations will be minuscule. More reliable observations of mass loss based on radio observations of CO, which make fewer assumptions on the dust component, indicate that mass-loss rates

are high – evidently something is needed to achieve these high mass-loss rates also in simulations.

The question is what happens when additional dust species are added to the simulations. Not all species are as transparent as forsterite. It seems valuable to study changes in the radiation field and wind driving mechanism where also enstatite is added and species that include iron, such as fayalite, ferrosilite and pure iron dust. Bladh & Höfner (2012) and also GS14 (see Chapter 12) argue that these minerals form much farther out than iron-free minerals, but it is still unknown what the result will be in a multi-fluid model where temperature gradients of drift models may be much steeper in the inner wind forming region (see Fig. 4i). Drift must not be ignored in stellar winds that are driven by minerals such as forsterite where extinction is dominated by scattering.

6. Conclusions

We have extended our frequency-dependent dust-driven high-spatial-resolution wind model code T-800 of Paper V with descriptions for mineral formation in oxygen-rich chemistry, as laid out by GS14. We have also calculated new opacity tables that are based on bound-bound cross sections of thirty [atoms and] molecules of the EXOMOL project and free-free and bound-free opacities of the JEKYLL code. With our improved model code and opacity data, we can choose molecular compositions and wavelengths freely and model stellar winds of both C-type and M-type stars that form various types of minerals. To our understanding, T-800 is the physically and numerically most detailed dynamic stellar wind code there is, and it is the only one that can accurately calculate effects of gas-to-dust drift in either type of star.

We have calculated models to explore effects of drift in M-type winds that are driven by forsterite particles. Extant studies favor this species as a wind driver. We selected model parameters of simulations that have shown high mass-loss rates. Our new PC models show a fair comparison with extant results (of H08 and B19); we cannot be more specific as details of those existing simulations are unavailable in the literature.

Differences are much larger when we compare results of PC models with drift models. Whilst changes in expansion velocities and grain sizes are modest, this is not so for the degree of condensation, dust-to-gas density ratio, and mass-loss rates. The drift velocity is 310–360 km s⁻¹ in the presented models; these high values result in very low degrees of condensation. The mass-loss rate is 7.5 times lower in one case and 21 times lower in a second case. The second model is important as is H08 used a model with the same parameters to prove the concept of stellar wind formation in M-type stars. Drift is more important in M-type stars than in C-type stars – the biggest difference is that momentum is transferred from the radiation field to the dust grains through scattering on transparent grains instead of through absorption in opaque grains.

More studies are needed that explore the use simultaneous formation of additional dust species to explain how observed high mass-loss rates form. And this cannot be done without drift – the resulting simulations is a multi-fluid problem. This article is a proof of concept of the influential effects of drift.

Acknowledgements. K.L.C. acknowledges funding from STFC, under project number ST/V000861/1. Parts of the computations were enabled by resources provided by the Swedish National Infrastructure for Computing (SNIC), partially funded by the Swedish Research Council through grant agreement no. 2018-05973. We thank B. Aringer (Vienna and Padova) for kindly providing us with an opacity table that we could use to develop and test our new model.

References

- Al Derzi, A. R., Furtenbacher, T., Tennyson, J., Yurchenko, S. N., & Császár, A. G. 2015, *J. Quant. Spectr. Rad. Transf.*, 161, 117
- Anders, E. & Grevesse, N. 1989, *Geochim. Cosmochim. Acta*, 53, 197
- Andersson, B. G., Lopez-Rodriguez, E., Medan, I., et al. 2022, *ApJ*, 931, 80
- Aringer, B. 2000, PhD thesis, Universität Wien
- Aringer, B., Girardi, L., Nowotny, W., Marigo, P., & Lederer, M. T. 2009, *A&A*, 503, 913
- Azzam, A. A., Tennyson, J., Yurchenko, S. N., & Naumenko, O. V. 2016, *MNRAS*, 460, 4063
- Barber, R. J., Strange, J. K., Hill, C., et al. 2014, *MNRAS*, 437, 1828
- Barlow, M. J. 1978, *MNRAS*, 183, 367
- Bernath, P. F. 2020, *J. Quant. Spectr. Rad. Transf.*, 240, 106687
- Bernath, P. F., Dodangodage, R., & Liévin, J. 2022, *ApJ*, 933, 99
- Bladh, S. & Höfner, S. 2012, *A&A*, 546, A76
- Bladh, S., Höfner, S., Aringer, B., & Eriksson, K. 2015, *A&A*, 575, A105
- Bladh, S., Höfner, S., Nowotny, W., Aringer, B., & Eriksson, K. 2013, *A&A*, 553, A20
- Bladh, S., Liljegren, S., Höfner, S., Aringer, B., & Marigo, P. 2019, *A&A*, 626, A100 (B19)
- Blommaert, J. A. D. L., de Vries, B. L., Waters, L. B. F. M., et al. 2014, *A&A*, 565, A109
- Bohren, C. F. & Huffman, D. R. 1983, *Absorption and scattering of light by small particles* (Wiley, New York)
- Brooke, J. S. A., Bernath, P. F., Western, C. M., et al. 2016, *J. Quant. Spectr. Rad. Transf.*, 168, 142
- Brooke, J. S. A., Ram, R. S., Western, C. M., et al. 2014, *ApJS*, 210, 23
- Chubb, K. L., Rocchetto, M., Yurchenko, S. N., et al. 2021, *A&A*, 646, A21
- Chubb, K. L., Tennyson, J., & Yurchenko, S. N. 2020, *MNRAS*, 493, 1531
- Coles, P. A., Yurchenko, S. N., & Tennyson, J. 2019, *MNRAS*, 490, 4638
- Coxon, J. A. & Hajigeorgiou, P. G. 2015, *J. Quant. Spectr. Rad. Transf.*, 151, 133
- Dorschner, J. 2010, in *Lecture Notes in Physics*, Berlin Springer Verlag, ed. T. Henning, Vol. 815, 1–60
- Dulick, M., Bauschlicher, C. W., Jr., Burrows, A., et al. 2003, *ApJ*, 594, 651
- Ergon, M. & Fransson, C. 2022, *A&A*, 666, A104
- Ergon, M., Fransson, C., Jerkstrand, A., et al. 2018, *A&A*, 620, A156
- Gail, H.-P. & Sedlmayr, E. 1999, *A&A*, 347, 594
- Gail, H.-P. & Sedlmayr, E. 2014, *Physics and Chemistry of Circumstellar Dust Shells*, 52 (Cambridge Univ. Press, New York) (GS14)
- Gautschi-Loidl, R., Höfner, S., Jørgensen, U. G., & Hron, J. 2004, *A&A*, 422, 289
- Gordon, I. E., Rothman, L. S., Hill, C., et al. 2017, *J. Quant. Spectr. Rad. Transf.*, 203, 3
- Grevesse, N. & Sauval, A. J. 1994, in *IAU Colloq. 146: Molecules in the Stellar Environment*, ed. U. G. Jørgensen, Vol. 428, 196–208
- Harris, G. J., Tennyson, J., Kaminsky, B. M., Pavlenko, Y. V., & Jones, H. R. A. 2006, *MNRAS*, 367, 400
- Höfner, S. 2008, *A&A*, 491, L1 (H08)
- Höfner, S., Bladh, S., Aringer, B., & Ahuja, R. 2016, *A&A*, 594, A108
- Höfner, S. & Olofsson, H. 2018, *A&A Rev.*, 26, 1
- Hubeny, I. & Mihalas, D. 2015, *Theory of Stellar Atmospheres* (Princeton Univ. Press, Princeton)
- Jäger, C., Dorschner, J., Mutschke, H., Posch, T., & Henning, T. 2003, *A&A*, 408, 193
- Krüger, D. & Sedlmayr, E. 1997, *A&A*, 321, 557
- Kurucz, R. & Bell, B. 1995, *Atomic spectral line database from CD-ROM 23 of R. L. Kurucz*, <https://lweb.cfa.harvard.edu/amp/ampdata/kurucz23/sekur.html>
- Li, G., Gordon, I. E., Le Roy, R. J., et al. 2013, *J. Quant. Spectr. Rad. Transf.*, 121, 78
- Li, G., Gordon, I. E., Rothman, L. S., et al. 2015, *ApJS*, 216, 15
- Lide, R. 1995, *CRC Handbook of Chemistry and Physics*, 78th edn. (CRC Press, Boca Raton, FL.)
- Liu, J., Jiang, B. W., Li, A., & Gao, J. 2017, *MNRAS*, 466, 1963
- Low, F. J. 1970, *Nature*, 227, 1333
- Masseron, T., Plez, B., Van Eck, S., et al. 2014, *A&A*, 571, A47
- Mattsson, L., De Cia, A., Andersen, A. C., & Petitjean, P. 2019, *A&A*, 624, A103
- Mattsson, L. & Sandin, C. 2021, *Universe*, 7, 113 (MS21)
- Mattsson, L., Wahlin, R., & Höfner, S. 2010, *A&A*, 509, A14
- Mattsson, L., Wahlin, R., Höfner, S., & Eriksson, K. 2008, *A&A*, 484, L5
- McKemmish, L. K., Masseron, T., Højeimakers, H. J., et al. 2019, *MNRAS*, 488, 2836
- McKemmish, L. K., Syme, A.-M., Borsovszky, J., et al. 2020, *MNRAS*, 497, 1081
- McKemmish, L. K., Yurchenko, S. N., & Tennyson, J. 2016, *MNRAS*, 463, 771
- Molster, F. J., Waters, L. B. F. M., & Kemper, F. 2010, in *Lecture Notes in Physics*, Berlin Springer Verlag, ed. T. Henning, Vol. 815, 143–201
- Molster, F. J., Waters, L. B. F. M., & Tielens, A. G. G. M. 2002, *A&A*, 382, 222
- Owens, A., Dooley, S., McLaughlin, L., et al. 2022, *MNRAS*, 511, 5448

- Paulose, G., Barton, E. J., Yurchenko, S. N., & Tennyson, J. 2015, *MNRAS*, 454, 1931
- Polyansky, O. L., Kyuberis, A. A., Zobov, N. F., et al. 2018, *MNRAS*, 480, 2597
- Roueff, E., Abgrall, H., Czachorowski, P., et al. 2019, *A&A*, 630, A58
- Rybicki, G. & Lightman, A. 1979, *Radiative Processes in Astrophysics* (WILEY-VCH Verlag, Weinheim)
- Sandin, C. & Höfner, S. 2003, *A&A*, 398, 253
- Sandin, C. & Höfner, S. 2004, *A&A*, 413, 789 (Paper III)
- Sandin, C. & Mattsson, L. 2020, *MNRAS*, 499, 1531 (Paper V)
- Sharp, C. M. & Huebner, W. F. 1990, *The Astrophysical Journal Supplement Series*, 72, 417
- Shemansky, D. E. 1969, *J. Chem. Phys.*, 51, 689
- Smirnov, A. N., Solomonik, V. G., Yurchenko, S. N., & Tennyson, J. 2019, *Physical Chemistry Chemical Physics (Incorporating Faraday Transactions)*, 21, 22794
- Somogyi, W., Yurchenko, S. N., & Yachmenev, A. 2021, *J. Chem. Phys.*, 155, 214303
- Späth, H. 1995, *Two Dimensional Spline Interpolation Algorithms* (A K Peters/CRC Press, New York)
- Syme, A.-M. & McKemmish, L. K. 2020, *MNRAS*, 499, 25
- Syme, A.-M. & McKemmish, L. K. 2021, *MNRAS*, 505, 4383
- Tennyson, J., Yurchenko, S. N., Al-Refaie, A. F., et al. 2020, *J. Quant. Spectr. Rad. Transf.*, 255, 107228
- Tosi, S., Dell’Aglia, F., Huerta-Martinez, E., & Ventura, P. 2022, *Universe*, 8, 270
- Underwood, D. S., Tennyson, J., Yurchenko, S. N., et al. 2016, *MNRAS*, 459, 3890
- Upadhyay, A., Conway, E. K., Tennyson, J., & Yurchenko, S. N. 2018, *MNRAS*, 477, 1520
- Uttenhaler, S., McDonald, I., Bernhard, K., Cristallo, S., & Gobrecht, D. 2019, *A&A*, 622, A120
- Verner, D. A., Ferland, G. J., Korista, K. T., & Yakovlev, D. G. 1996, *ApJ*, 465, 487
- Verner, D. A. & Yakovlev, D. G. 1995, *A&AS*, 109, 125
- Western, C. M. 2017, *J. Quant. Spectr. Rad. Transf.*, 186, 221
- Western, C. M., Carter-Blatchford, L., Crozet, P., et al. 2018, *J. Quant. Spectr. Rad. Transf.*, 219, 127
- Whitelock, P. A., Menzies, J. W., Feast, M. W., et al. 2009, *MNRAS*, 394, 795
- Wickramasinghe, N. C. 1972, *MNRAS*, 159, 269
- Wolf, N. J. & Ney, E. P. 1969, *ApJ*, 155, L181
- Yousefi, M., Bernath, P. F., Hodges, J., & Masseron, T. 2018, *J. Quant. Spectr. Rad. Transf.*, 217, 416
- Yurchenko, S. N., Al-Refaie, A. F., & Tennyson, J. 2018a, *A&A*, 614, A131
- Yurchenko, S. N., Amundsen, D. S., Tennyson, J., & Waldmann, I. P. 2017, *A&A*, 605, A95
- Yurchenko, S. N., Mellor, T. M., Freedman, R. S., & Tennyson, J. 2020, *MNRAS*, 496, 5282
- Yurchenko, S. N., Szabó, I., Pyatenko, E., & Tennyson, J. 2018b, *MNRAS*, 480, 3397
- Yurchenko, S. N. & Tennyson, J. 2014, *MNRAS*, 440, 1649
- Yurchenko, S. N., Tennyson, J., Syme, A.-M., et al. 2022, *MNRAS*, 510, 903

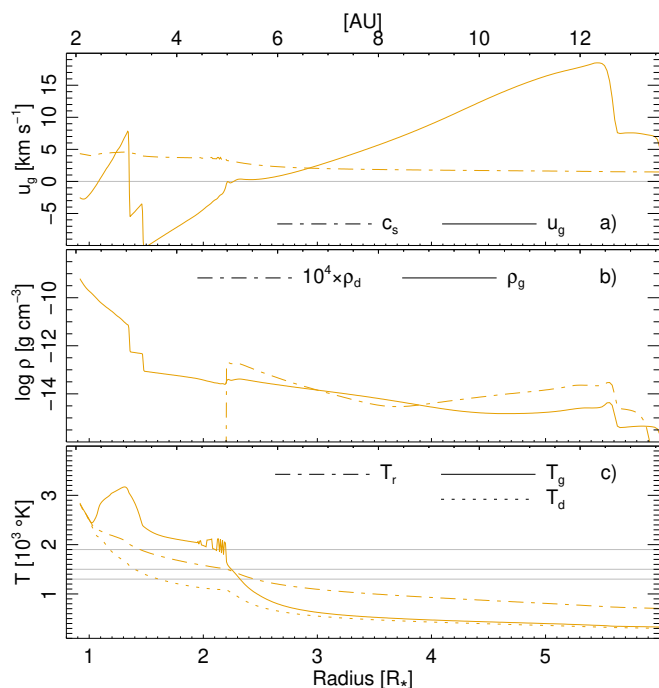


Fig. B.1. Radial structure of a snapshot of setup L3.85T24 for the inner modelled region. A PC model using the gas opacities of Aringer is shown with orange lines. The 3 panels show: (a) gas velocity u_g , sound speed c_s ; (b) gas density ρ_g , dust density $10^4 \times \rho_d$ (log); and (c) gas temperature T_g , radiative temperature T_r , and dust temperature T_d . All properties are drawn versus the stellar radius R_* (lower axis) and astronomical units (AU; upper axis). Grey horizontal lines are guides.

Appendix A: Calculation of the bound-free opacity

Here is a brief description of the methods and data used in the determination of the bound-free opacity, which is calculated using the `JEKYLL` code (Ergon et al. 2018; Ergon & Fransson 2022). As in the calculations of our bound-bound opacities, we first determine cross sections of bound-free level populations and then calculate opacities based on the physical conditions.

The photo-ionization cross-sections for ground states are calculated using analytic fits of Verner & Yakovlev (1995) and Verner et al. (1996), and for the lowest excited states of He I, C I, O I, Mg I, Mg II, Si I, S I, and Ca II, using data from TOPBASE of the Opacity Project⁶. For all other excited states, the photo-ionization cross-sections are calculated using a hydrogenic approximation by Rybicki & Lightman (1979).

The bound-free opacity is then calculated based on LTE populations of excited and ionized states for given values of density, temperature, and composition. The atomic data (excitation and ionization energies and statistical weights) are obtained from the Atomic Spectra Database of NIST⁷ and the online tables by R. Kurucz⁸.

Appendix B: On the role of the gas opacity data

Developing our new oxygen-rich chemistry models we calculated test wind models using the same gas opacity table that B19 use (Aringer 2000; Aringer et al. 2009, the data are described in). The first test models indicated a problem when starting the stellar wind; some kind of noise appears in the gas temperature

of all models when dust is present and where $T_g \approx 2000$ K. We show an example of such noise in Fig. B.1, which presents a snapshot of a stellar wind model where calculations have just begun. The noise occurs in the temperature in the interval $1.9 \lesssim r \lesssim 2.2 R_*$. The same noise is [spatially] unresolved in models using $N_d = 100$ grid points (not shown), and here, the problem is much smaller. The problem becomes prohibitive in drift models, which are more sensitive to variations of this kind. The origin of the noise is unknown, but no terms in the radiation hydrodynamic equations appear to be responsible considering the noise always appears at the same gas temperature. Therefore, we hypothesized that the noise originate in the gas opacity data.

We calculated new gas opacity tables based on EXOMOL data, as we describe in Sect. 4.2.1. The extant and new opacity data sets are compared in Fig. B.2, for the wavelength $\lambda = 1 \mu\text{m}$. The figures show large differences at all temperatures but the lowest where the offset is about 0.7 dex. Differences are also larger at lower densities. At higher temperatures and lower densities our new bound-bound opacities drop faster to low values. The same low values are not seen in the opacity data of Aringer et al., whose opacity values at the higher temperatures $T \gtrsim 4000$ K are up to 10^8 times higher than our values. In our new opacities, data at these higher temperatures are completely dominated by the free-free and bound-free components that show structure at the lower densities ($\rho \lesssim 10 \times 10^{-10} \text{ g cm}^{-3}$). The opacity data of Aringer et al. show values that appear to be more constant at higher temperatures and lower densities; their data show much less structure than our new opacities.

With our new opacities, the stellar wind calculations are not hampered by the noise at $T \approx 2000$ K described above. The extant opacity tables only allow is to speculate on why these data give rise to noise in the temperature when we use them to attempt to calculate a stellar wind. Our guess is that the problem is connected to the much higher values on the opacities throughout the parameter domains.

⁶ <http://cdsweb.u-strasbg.fr/topbase/topbase.html>

⁷ <https://www.nist.gov/pml/atomic-spectra-database>

⁸ <https://lweb.cfa.harvard.edu/amp/ampdata/kurucz23/sekur.html>

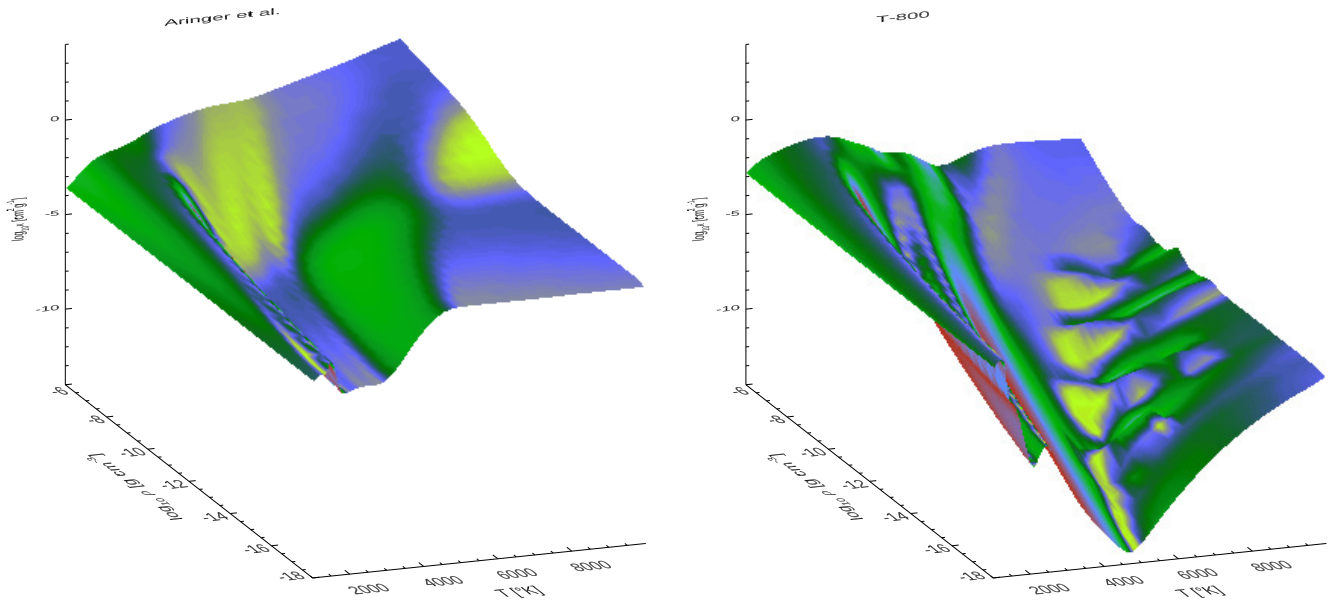


Fig. B.2. The total gas opacity at the wavelength that is the closest to $\lambda = 1\mu\text{m}$ for the data of Aringer et al. (left panel) and our new data (right panel). The opacity (z -axis) is shown versus the temperature (x -axis) and the gas density (y -axis). The temperature and density ranges are $1000 \leq T \leq 10\,000$ K and $-18 \leq \log \rho \leq -6$ g cm $^{-3}$, respectively. The two panels use the same ranges on all three axes.